

PACS numbers: 52.38.Mf; 81.16. – c
DOI: 10.1070/QE2009v039n06ABEH013981

Laser ablation plume dynamics in nanoparticle synthesis

V.V. Osipov, V.V. Platonov, V.V. Lisenkov

Abstract. **The dynamics of the plume ejected from the surface of solid targets (YSZ, Nd : YAG and graphite) by a CO_2 laser pulse with a duration of ~ 500 μs (at the 0.03 level), energy of 1.0 – 1.3 J and peak power of 6 – 7 kW have been studied using high-speed photography of the plume luminescence and shadow. The targets were used to produce nanopowders by laser evaporation. About 200 μs after termination of the pulse, shadowgraph images of the plumes above the YSZ and Nd : YAG targets showed dark straight tracks produced by large particles. The formation of large (~ 10 μm) particles is tentatively attributed to cracking of the solidified melt at the bottom of the ablation crater. This is supported by the fact that no large particles are ejected from graphite, which sublimes without melting. Further support to this hypothesis is provided by numerical 3D modelling of melt cooling in craters produced by laser pulses of different shapes.**

Keywords: *laser plume, laser ablation, nanoparticles.*

1. Introduction

In recent years, ever increasing attention has been paid to studies concerned with nanomaterials engineering. Nanopowders are a key component of such materials. There are many physical and chemical nanopowder production methods [1], among which laser evaporation of solid targets holds a special position. The advantages of this method (sometimes referred to as laser synthesis of nanopowders) were formulated by Muller et al. [2]: weak agglomeration of nanoparticles, the possibility of producing multicomponent nanopowders with relative ease, freedom from contaminating processes, small nanoparticle size and narrow size distribution. The method, however, has not only advantages but also drawbacks. As shown previously [3], the powders synthesised by this method consist of three types of particles: spherical particles 2 – 40 nm in size (weight fraction 9 % – 97 %), spherical particles 0.2 – 2.0 μm in size (weight fraction 3 % – 7 %) and 5- to 10-μm particles of arbitrary shape. As distinct from the nanoparticles, the large spherical and irregularly shaped particles are identical in chemical and phase compositions to the solidified melt on the target surface. Moreover, even larger (~ 100 μm) particles were found on the walls of the evaporation chamber. Such particles were not entrained by the gas flow over the target surface, intended to transport nanoparticles into a mechanical filter collector.

Recent work [4] has shown that, during sintering of laser-synthesised Nd : Y_2O_3 powders, spherical particles do not impede the formation of homogeneous crystallites needed to obtain transparent ceramics, whereas irregularly shaped large particles, with a sharply reduced Laplace pressure on their surface, are surrounded by pores, which have an adverse effect on the optical transmission of the ceramic.

To eliminate large particles, the process must include a costly sedimentation step capable of removing all the particles greater than 200 nm in size. Given the above, the objective of this research was to find out how irregularly shaped large particles form during nanopowder synthesis. To this end, the laser ablation plume was visualised using high-speed photography and shadowgraph imaging, capable of pinpointing when and where large particles appear. To gain insight into the processes involved, we solved the three-dimensional (3D) heat equation.

2. Experimental setup

High-speed photographs of the laser ablation plume and its shadow were taken in air at atmospheric pressure and room temperature. The radiation source was a repetitively pulsed LAERT CO_2 laser, capable of producing 10.6-μm pulses up to 1.3 J in energy and up to ~ 10 kW in peak power at a repetition rate of 500 Hz [5]. In our experiments, the laser was operated in a single-pulse regime, with a pulse energy of 1.0 – 1.3 J and a peak power of 6 – 7 kW. A typical oscilloscope trace of the laser pulse is presented in Fig. 1. Ablation targets were fabricated by pressing yttria-stabilised zirconia (YSZ) powder and an appropriate Nd : YAG oxide mixture, followed by sintering at 1300 °C for 8 h. In addition, we used a pyrolytic graphite target.

These target materials were chosen because YSZ is widely used in solid oxide fuel cell technology and transparent Nd : YAG ceramics are used as active media of solid-state lasers. Both materials vaporise from the melt. The choice of pyrolytic graphite was prompted by the fact that this material sublimes without melting. The reasons for this choice will be explained in detail below.

V.V. Osipov, V.V. Platonov, V.V. Lisenkov Institute of Electrophysics, Ural Branch, Russian Academy of Sciences, ul. Amundsena 106, 620016 Yekaterinburg, Russia; e-mail: osipov@iep.uran.ru, max@iep.uran.ru, lisenkov@iep.uran.ru

Received 20 July 2008; revision received 10 February 2009
Kvantovaya Elektronika **39** (6) 541 – 546 (2009)
Translated by O.M. Tsarev

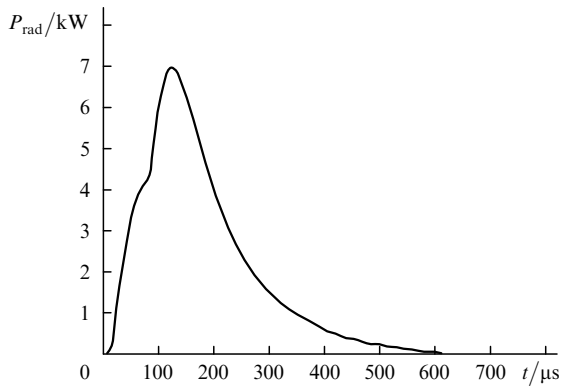

Figure 1. Shape of LAERT CO_2 laser pulses.

In all our experiments, the laser beam was directed to the target at 45° to the surface normal and was focused by a potassium chloride lens with a focal length of 107 mm to an elliptical spot with axes of 0.9 and 0.75 mm. The peak power density incident on the target was 1 – 1.3 MW cm^{-2}. After each pulse, the target was translated by a mechanical drive so that the next pulse encountered a virgin surface.

The shape and temporal evolution of the luminous zone in the laser plume were examined using a VFU-1 high-speed video camera. During a single CO_2 laser pulse, a series of plume images were taken at frame intervals of 15.5 μs and exposure times of ~ 1 μs.

To explore the temporal and spatial evolution of the ablation plume after cooling of the laser plasma, when the plasma luminescence had died out, the shadowgraph method was used. Shadowgraph images were obtained with the experimental setup shown schematically in Fig. 2, which incorporated a quartz lens system, 1-mm-diameter aperture, 337-nm coherent radiation source (AIL-0.5 nitrogen laser) and SensiCam FastShutter VGA b/w CCD camera. With this setup, we were able to capture one frame from a single CO_2 laser pulse, with a controlled time delay from 0 to 100 ms relative to the plume initiation at the target. The exposure time was set by the nitrogen laser pulse width (full width at half-maximum, 5 ns). To ensure data reproducibility and identify the instant when the plume appeared, the integrated luminescence intensity of the laser plasma was monitored with a FEK-22 photomultiplier. Only those shadowgraph images were analysed which corresponded to identical FEK-22 signals.

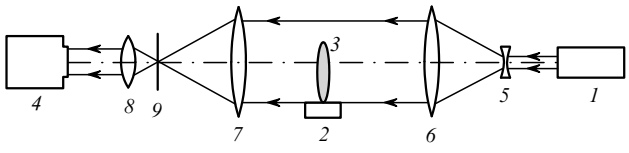

Figure 2. Schematic of the experimental setup for shadowgraph imaging of the laser ablation plume: (*1*) N_2 laser, (*2*) target, (*3*) laser plume, (*4*) CCD camera, (*5–8*) quartz lenses, (*9*) aperture.

3. Experimental results and discussion

With all the target materials tested, the ablation plume propagated along the surface normal even though the laser beam was incident at 45° to the target surface. Therefore, no optical breakdown developed in the vapour phase.

The ablation plume above the YSZ target appeared 25 μs after the beginning of the laser pulse. That time was needed to melt the target material and to bring the melt to the boiling point. The luminous zone in the plume (Fig. 3) had a needle-like shape. Its initial diameter (0.5 mm) was smaller than the beam spot size, and its maximum diameter (~ 2 mm) was reached 130 μs after the onset of target vaporisation. The height of the luminous zone correlated rather well with the instantaneous incident laser beam power. Near the top of the laser pulse, the plume length reached a maximum (22 mm). At the trailing edge of the pulse, the plume length dropped and the luminous zone disappeared.

In a previous study [6], the luminous zone of the laser plume was shown to consist mainly of YO and ZrO radicals. The temperature of ions and neutrals near the target surface was 4.6 kK, which is close to the boiling point of YSZ (4.57 kK), whereas 7 mm from the target the molecular temperature of the plume dropped to 3.1 kK. At the same time, farther away from the target surface the temperature increased again, reaching 3.7 kK at a distance of 12 mm. The local rise in temperature was associated with the onset of vapour condensation, accompanied by nanoparticle growth and heat release.

Shadowgraph images typical of particular delay times are shown in Fig. 3. They provide insight into the dynamics of all the zones in the plume, including the non-luminous one. At the leading edge of the laser pulse, the plume is column-shaped, like its luminous zone. The leading plume edge propagates in air at a velocity of ~ 220 m s^{-1}. It is preceded by a compressed air layer, which results in a weak shock wave. After 200 μs, i.e. on the trailing side of the laser pulse, the plume becomes mushroom-shaped: 4 – 6 mm from the target surface, a 'mushroom cap' consisting of many vortex structures begins to form and gradually moves away from the target. The distance where most vortices are formed correlates well with spectroscopic data on the condensation onset. Most likely, the vortices consist of a mixture of condensing vapour, nanoparticles and air. Analysis of transmission electron microscopy (TEM) images indicates that 93 % – 97 % of the laser-ablated material condenses in the form of spherical particles ~ 10 nm in average size, in good agreement with previous results [3].

Starting at 844 μs (i.e. approximately 200 μs after termination of the pulse) and up to 5 ms, the images show dark straight bands issuing from the ablation crater. We suppose that these are the tracks of large particles ejected from the bottom of the crater. The above data can be used to roughly estimate the ejection velocity of such particles: we obtain tens of metres per second. Characteristically, all large particles that produce tracks are ejected at various angles in the half-plane opposite to that where the laser beam is incident on the target. The causes of this behaviour are not yet clear.

It seems unlikely that the tracks observed in the shadowgraph images result from melt ejection: the tracks appear after termination of the pulse, when there is no target vaporisation and the vapour pressure in the crater is not very high. None of the shadowgraph images obtained during the laser pulse shows tracks. The photographs of the plume luminescence also do not show any ejected particles.

One possible reason for track formation is as follows: Since a solid and its melt as a rule differ in density,

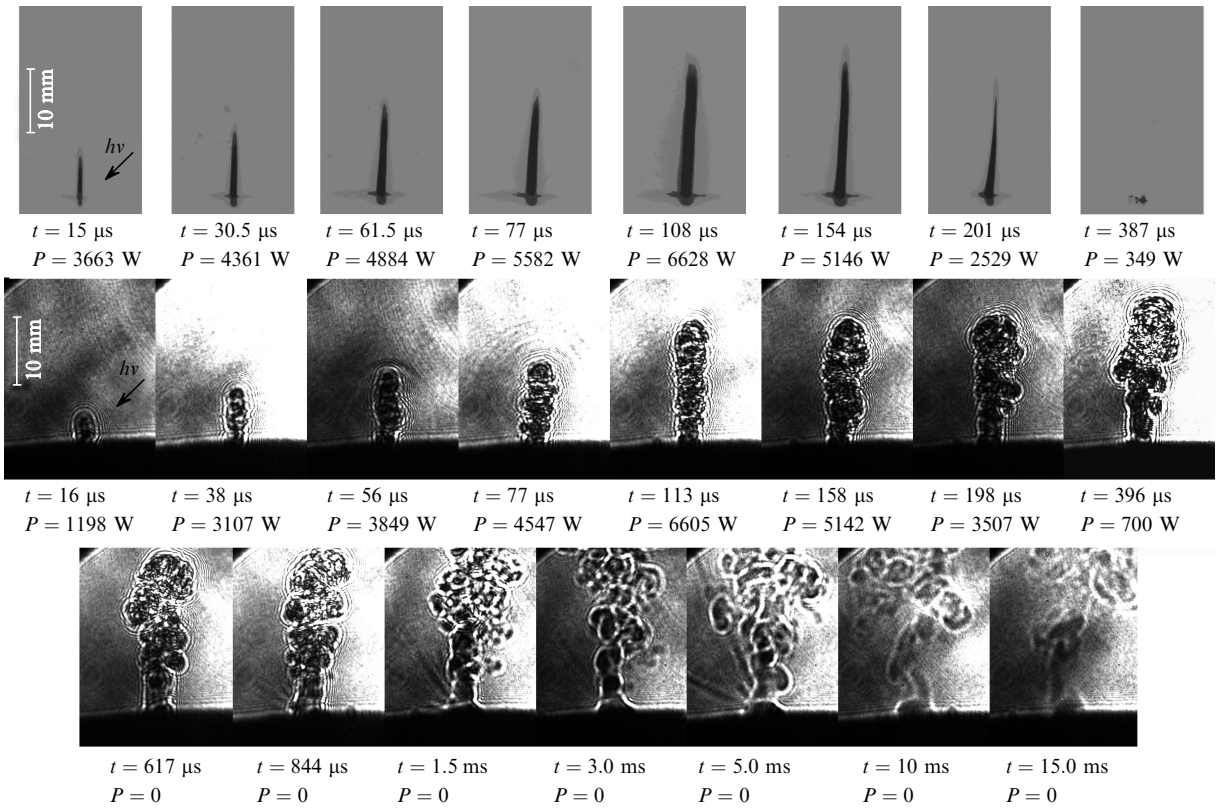

Figure 3. Photographs (upper row) and shadowgraph images (two lower rows) of the laser ablation plume above the YSZ target. The time is measured from the instant of plume initiation; P is the instantaneous incident CO_2 laser beam power.

solidification of the melt pool gives rise to considerable stress and, accordingly, cracking. Because the bottom of the crater is inhomogeneous, there appear forces that eject pieces of the solidified material into the carrier gas flow.

If this assumption is true, large particles must always appear when the target material melts, and there will be no such particles when ablation leads to sublimation of the target material without melting. To verify this hypothesis, we tested targets of Nd : YAG and pyrolytic graphite. The latter undergoes a solid vapour phase transition, without melting, at a temperature of ~ 4800 K, corresponding to the triple point in its phase diagram.

Shadowgraph images of the ablation plume above the Nd : YAG target (Fig. 4a) demonstrate qualitatively the same plume expansion dynamics as in the case of the YSZ target, with ejection of large particles from the crater region. Like in the images of the YSZ target, a shock wave is well seen. Its velocity is ~ 450 m s^{-1} during the first 17 μs and drops to 375 m s^{-1} over the next 20 μs. Moreover, there is a track produced by a rather large particle, which is likely to have traversed the carrier gas flow and reached the wall of the evaporation chamber rather than having been entrained to the filter.

Radically different behaviour of the ablation plume was observed with the pyrolytic graphite target. None of the images obtained (including those not shown in Fig. 4b) showed tracks of large particles. Given that this finding had important implications for subsequent analysis, it was verified further. To this end, the resultant carbon nanopowder was collected on a mechanical filter and examined by TEM. One of its micrographs is presented in Fig. 5a. The powder is seen to consist of highly agglomerated, nearly spherical particles. Figure 5b shows the particle size distribution of the powder. The distribution is rather narrow, with a full width of ~ 40 nm. The geometric mean particle size is 11.7 nm. The specific surface area of the carbon nanopowder is 439 m^2 g^{-1} as determined by BET measurements, and the nanopowder contains no large particles.

Thus, all the above data suggest, albeit indirectly, that the formation of irregularly shaped large particles is associated with cracking of the solidified melt. Further insight into the origin of such particles can be gained by numerically modelling the melting, vaporisation and solidification processes in the beam spot on the target surface.

To analyse these processes, we solved the 3D heat equation

$$c(T)\frac{\partial T}{\partial t} = \nabla(\kappa \nabla T) + Q_{\text{in}}, \tag{1}$$

where c is volumetric heat capacity; κ is thermal conductivity; and Q_{in} is the internal heat source term. To simplify the problem, κ was taken to be temperature-independent. The equation then has the form

$$\frac{\partial T}{\partial t} = \chi(T)\Delta T + \frac{Q_{\text{in}}}{c(T)}, \tag{2}$$

where χ is thermal diffusivity.

A laser beam travelling along the z axis and striking the xy surface of a target creates a 3D heat source with a power density

$$Q_{\text{in}} = \alpha I(x, y, z, t), \tag{3}$$

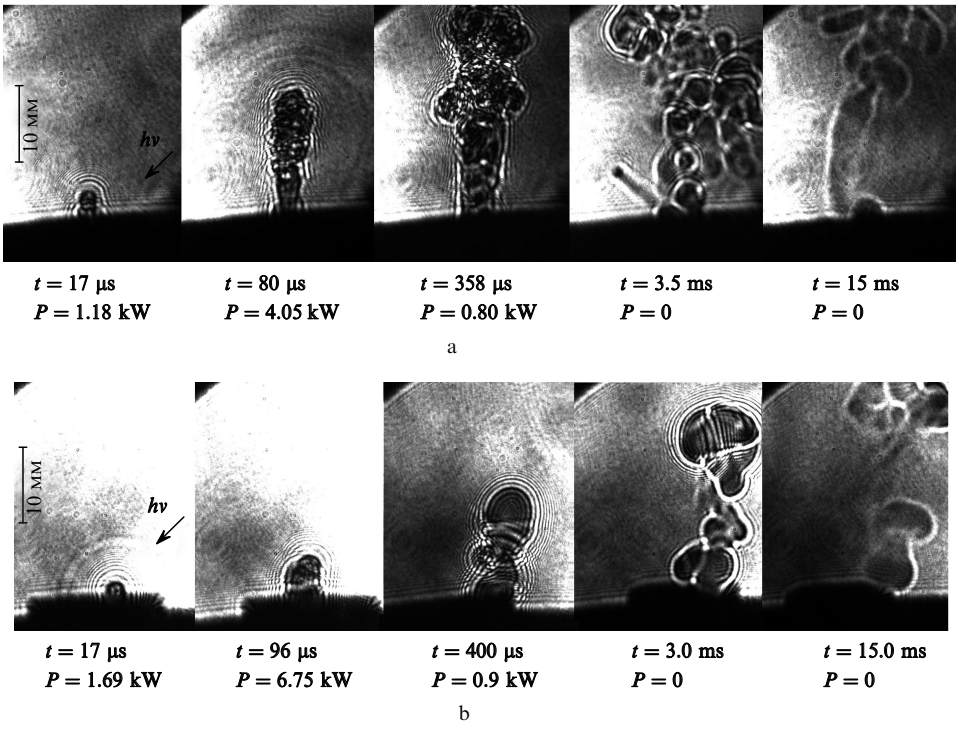

Figure 4. Shadowgraph images of the laser ablation plume above the (a) Nd : YAG and (b) graphite targets. The time is measured from the instant of plume initiation.

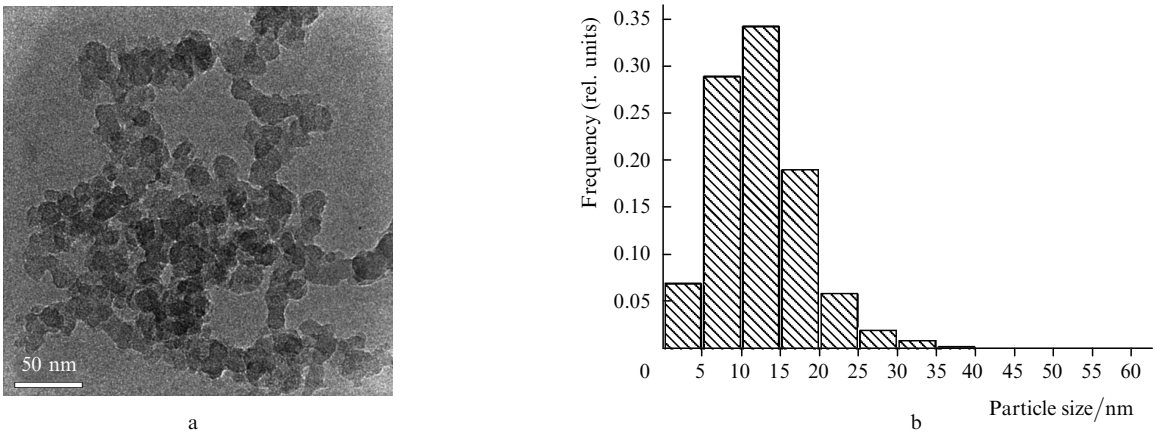

Figure 5. (a) SEM micrograph and (b) size distribution of carbon nanoparticles produced by ablation of graphite.

where α is the absorption coefficient for the laser radiation;

$$I(x, y, z, t) = (1 - R)I_o(x, y)f(t)\exp(-\alpha z) \quad (4)$$

is the intensity distribution in the material; $I_o(x, y)$ is the focal-spot intensity distribution; R is the reflectance of the target; and $f(t)$ is a time-dependent form factor.

The focal-spot intensity distribution $I_o(x, y)$ is shown in Fig. 6a. It approximates rather well the experimental data in Fig. 6b. The reflectance of the target surface was estimated from the depth of the ablation crater produced on the target by a single laser shot and from the amount of material evaporated by the shot. The pulse shape and peak power were the same as in that experiment (Fig. 1). On the whole, the modelling procedure we used follows a generally accepted approach described in various forms in well-known books [7–9]. One simplification is that we do not take into account that the melt is expelled by the target material vapour overpressure in the ablation plume. This is justified by the fact that, at the incident intensities used in this study, a significant fraction of the melt vaporises before being expelled from the laser heating zone, in contrast to the well-known deep-penetration (keyhole) melting regime. Therefore, most of the material is ejected from the crater not as liquid but as vapour, as supported by solid experimental evidence [3, 4]. In addition, as determined by atomic force microscopy the crater depth is 10–15 μm, which far exceeds the lateral dimensions of the crater ($\sim 0.9 \times 0.7$ mm). Note that we are particularly interested in the final stage of the laser pulse, where the overpressure is nearly zero, and the melt is not expelled by the vapour.

The model above was used to simulate the dynamics of the temperature field around the focal spot, with the simplification that the melting and solidification processes

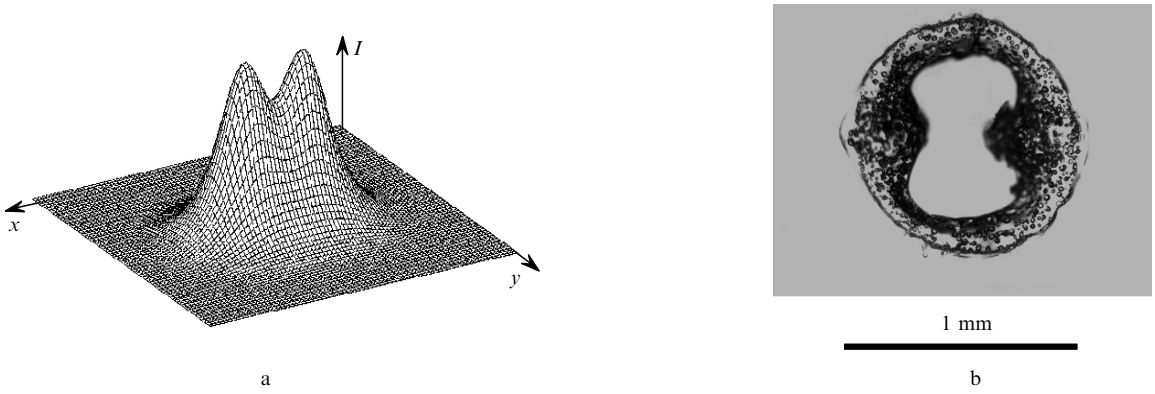

Figure 6. (a) Focal-spot intensity distribution used in numerical simulation; (b) beam spot at normal incidence.

during heating and cooling to the melting point were taken to be instantaneous. The melting temperature of the YSZ target was taken to be 3173 K (the same as that of ZrO_2). Its specific heat of fusion was included in its heat capacity and evenly distributed over the temperature range 300 – 3173 K.

These data are presented in Fig. 7 as isotherms and in Fig. 8 as melt profiles at different instants of time. In both figures, the melt pool is shown grey. Since we are interested only in the behaviour of the melt, the z coordinate is measured downwards from the melt surface after evaporation. The melt has the maximum surface area at $t = 350$ μs (Figs 7, 8). Subsequently, melt solidification at the periphery of the pool, resulting in a reduction in melt volume, is accompanied by in increase in melt depth at the maxima in incident intensity. Solidification also begins in the central part of the target: by $t = 800$ μs, the melt pool divides into two parts. Afterwards, the two pools decrease in both volume and depth.

Thus, the simulation results suggest that melt solidification begins about 350 μs after the beginning of laser irradiation. At the same time, in our experiments the first large particles were detected in the ablation plume 800 μs after the onset of target vaporisation, i.e. ~ 200 μs after termination of the pulse. According to the simulation results, it is at this point in time that the melt pool divides into two parts and the isotherms are most severely distorted, so that both the temperature field and its gradient are nonuniform. These factors may be responsible for the ejection of the first large particles. Subsequently, because no target vaporisation occurs, the thickness and surface area of the solidified melt increase, as does the probability of cracking in other places of the crater. Clearly, to reduce the number of large particles the incident intensity must have a uniform distribution, which will reduce the surface area and depth of the melt.

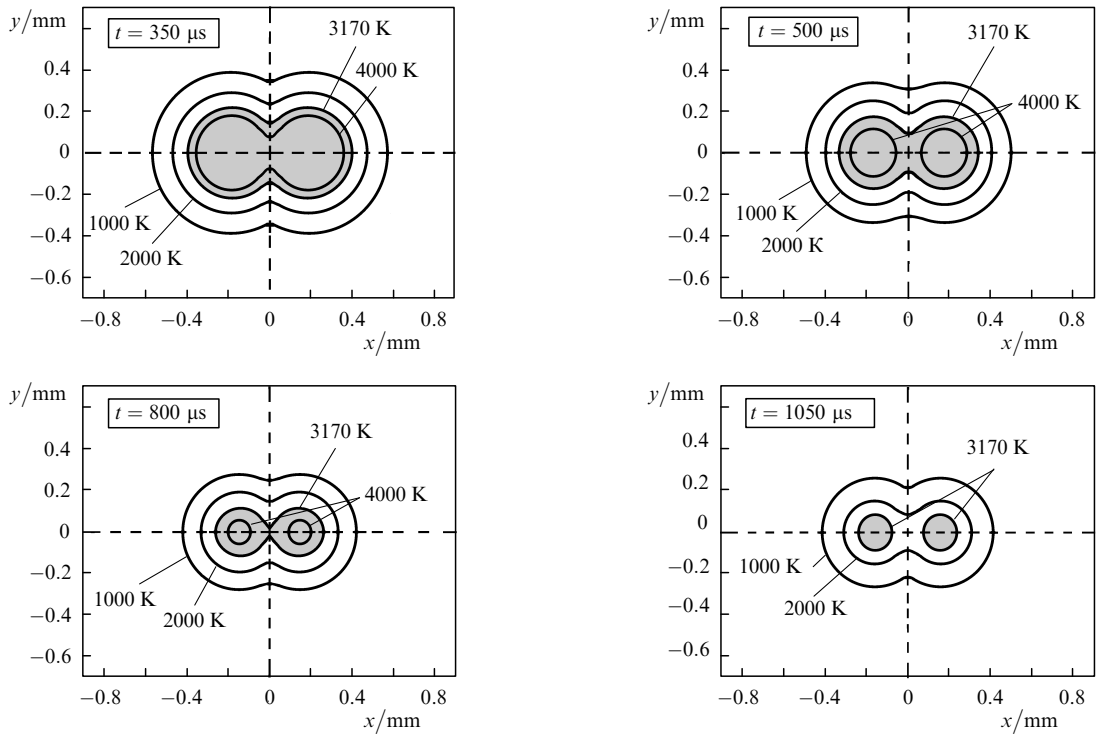

Figure 7. Temperature fields on the target surface at different instants of time after exposure to a single laser pulse. The melt pool is shown grey.

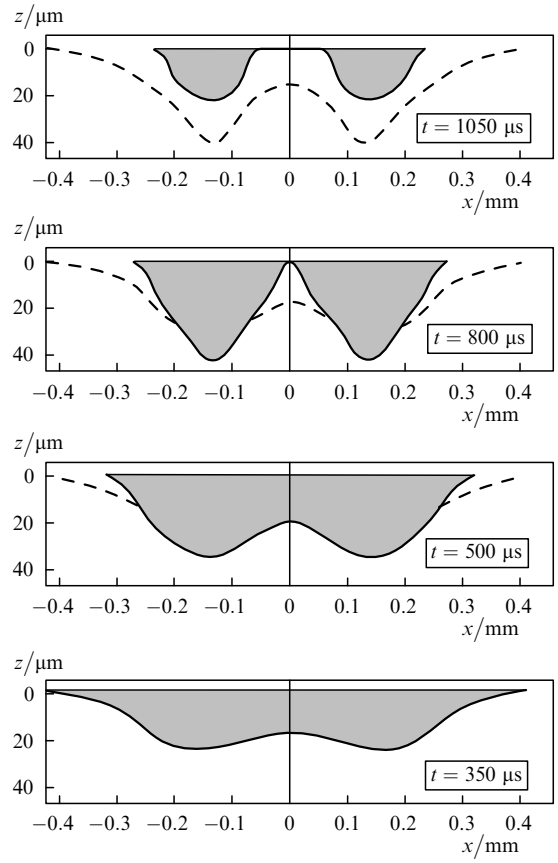

Figure 8. Melt profiles in a target at different instants of time after exposure to a single laser pulse. The melt pool is shown grey, and the dashed curves represent the boundaries of the melt solidified by the given time.

4. Conclusions

After exposure to a laser pulse, large particles (5–100 μm) have been detected in the ablation plume above the target. In shadowgraph images, such particles produce dark straight tracks issuing from the ablation crater. The first large particles appear ~ 200 μs after termination of the pulse, and the process lasts several milliseconds.

The formation of large particles is tentatively attributed to cracking of the solidified melt at the bottom of the ablation crater. This is supported by the results obtained with a graphite target, which sublimes without melting, and by numerical 3D modelling of the melt dynamics.

Acknowledgements. This work was supported by the Russian Foundation for Basic Research (Grant No. 08-02-99056 r_ofi) and by the Presidium of the Ural Branch of the Russian Academy of Sciences.

References

1. Gusev A.I. *Nanomaterialy, nanostruktury, nanotekhnologii* (Nanomaterials, Nanostructures and Nanotechnologies) (Moscow: Fizmatlit, 2005).
2. Muller E., Ostereich Ch., Popp U., et al. *J. KONA – Powder and Particle*, (13), 79 (1995).
3. Osipov V.V., Kotov Yu.A., Ivanov M.G., et al. *Laser Phys.*, **16**, 116 (2006).
4. Osipov V.V., Ivanov V.V. *Proc. X111 Int. Conf. Methods Aerophys. Research* (Novosibirsk: Parallel', 2007) part II.
5. Osipov V.V., Ivanov M.G., Lisenkov V.V., Platonov V.V. *Kvantovaya Elektron.*, **32**, 253 (2002) [*Quantum Electron.*, **32**, 253 (2002)].
6. Osipov V.V., Solomonov V.I., Platonov V.V., et al. *Kvantovaya Elektron.*, **35**, 633 (2005) [*Quantum Electron.*, **35**, 633 (2005)].
7. Vedenov A.A., Gladush G.G. *Fizicheskie protsessy pri lazernoi obrabotke materialov* (Physical Processes Underlying Laser Processing of Materials) (Moscow: Energoatomizdat, 1985).
8. Duley W. *Laser Processing and Analysis of Materials* (New York: Plenum, 1983; Moscow: Mir, 1986).
9. Prokhorov A.M., Konov V.I., Ursu I., Mikheilesku I.N. *Vzaimodeistvie lazernogo izlucheniya s metallami* (Interaction of Laser Radiation with Metals) (Moscow: Nauka, 1988).